

## Effect of sea ice rheology in numerical investigations of climate

Jinlun Zhang and D. A. Rothrock

Polar Science Center, Applied Physics Laboratory, College of Ocean and Fishery Sciences, University of Washington, Seattle, Washington, USA

Received 15 July 2004; revised 8 March 2005; accepted 27 May 2005; published 31 August 2005.

[1] Plastic sea ice rheologies that employ teardrop and parabolic lens yield curves and allow varying biaxial tensile stresses have been developed. These rheologies, together with the previously developed ellipse and Mohr-Coulomb-ellipse rheologies, are implemented in a thickness and enthalpy distribution sea ice model to examine the rheological effect in numerical investigations of arctic climate. The teardrop, lens, and ellipse rheologies obey a normal flow rule and result in a two-peak shear stress distribution. The first peak is at the zero shear stress; the second is near  $16,000 \text{ N m}^{-1}$  for the ellipse and two lens rheologies and near  $30,000 \text{ N m}^{-1}$  for the two teardrop rheologies. The location of the second peak depends on the fatness of the yield curve and the amount of biaxial tensile stress allowed. In contrast, the Mohr-Coulomb-ellipse rheology, based on Coulombic friction failure, does not tend to create the second peak. The incorporation of biaxial tensile stress tends to increase ice thickness in most of the Arctic. A fatter yield curve tends to increase the frequency of large shear stresses. An increased frequency of large shear stresses, in conjunction with the inclusion of biaxial tensile stress, tends to reduce ice speed and ice export, to enhance ice ridging in the Arctic interior, and to reduce ice ridging in the coastal areas, which has a significant impact on arctic spatial ice mass distribution and the total ice budget. The teardrop rheologies reduce spatial bias of modeled ice draft against submarine observations more than others. By changing ice motion, deformation, and thickness the choice of plastic rheology also considerably affects the simulated surface energy exchanges, particularly in the Arctic marginal seas.

**Citation:** Zhang, J., and D. A. Rothrock (2005), Effect of sea ice rheology in numerical investigations of climate, *J. Geophys. Res.*, 110, C08014, doi:10.1029/2004JC002599.

### 1. Introduction

[2] In many regional or global climate models that include sea ice dynamics, ice motion is described by a momentum equation that treats the ice cover as a two-dimensional continuum obeying a certain constitutive law, or rheology. Ice rheology describes ice internal interaction that is recognized to be a complicated physical process of high nonlinearity. Two plastic rheologies have predominated in sea ice models; the elastic-plastic rheology [Coon, 1974; Pritchard, 1975] and viscous-plastic rheology [Hibler, 1979]. The viscous-plastic rheology has been used widely in large-scale sea ice modeling because of the subsequently development of numerical methods that solve efficiently the momentum equation employing this rheology. These include the point successive relaxation (PSR) method [Hibler, 1979], the line successive relaxation (LSR) method [Zhang and Hibler, 1997], the elastic-viscous-plastic (EVP) method [Hunke and Dukowicz, 1997], and the alternating direction implicit (ADI) method [Zhang and Rothrock, 2000]. In particular, the EVP and LSR ice dynamics solvers

have been found useful for parallel computing [Hunke and Zhang, 1999; Zhang and Rothrock, 2003]. Recently, we have coupled a parallel dynamic thermodynamic sea ice model, employing either the LSR or the ADI solver, to the Massachusetts Institute of Technology ocean general circulation model (MITgcm) (see <http://mitgcm.org>) for wider application including data assimilation [Menemenis *et al.*, 2005].

[3] With ice strength given, a viscous-plastic rheology is mainly determined by (the shape of) a plastic yield curve and a flow rule. Although previous studies [Ip *et al.*, 1991; Ip, 1993] implemented sine lens, square, and capped Mohr-Coulomb yield curves, perhaps the most widely used plastic rheology for climate studies consists of an ellipse yield curve (Figure 1) along which a normal flow rule is enforced [Hibler, 1979]. Recently, Hibler and Schulson [1997] developed a model by taking sea ice as a composite system that consists of strong thick ice embedded with weak thin ice leads. They were able to achieve "isotropic realizations" by dynamically treating oriented thin ice leads so that the basic characteristics of ice flaws were captured using isotropic rheologies. One realization led to a lens-like plastic yield curve, another to a teardrop-like curve. Use of the teardrop yield curve [Rothrock, 1975] has, to our

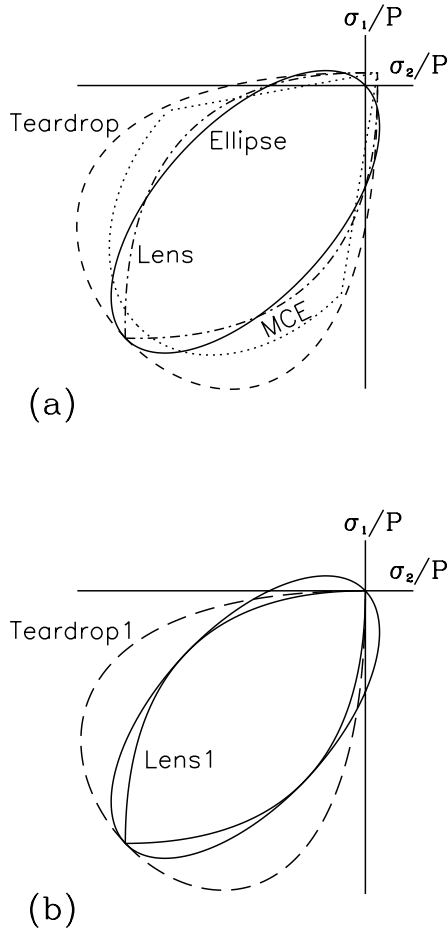


**Figure 1.** Six plastic yield curves in normalized principal stress space: (a) the yield curves that allow tensile stress and (b) the ellipse yield curve shown with those that do not allow tensile stress.

knowledge, never been implemented for large-scale sea ice simulations. The work of *Hibler and Schulson* [1997] raises our interest in formulating and using a teardrop constitutive law.

[4] *Hibler and Schulson* [2000] derived a plastic yield curve based on Coulombic-like friction failure. This yield curve is a combination of an ellipse yield curve where the normal flow rule applies and a Mohr-Coulomb yield curve where the normal flow rule does not apply (Figure 1). In line with laboratory observations [e.g., *Schulson*, 2001], the Mohr-Coulomb-ellipse (MCE) yield curve allows a certain amount of biaxial tensile stress, which differs from tension-free granular Coulombic yield curves [*Smith*, 1983; *Overland and Pease*, 1988; *Tremblay and Mysak*, 1997] as well as the capped Mohr-Coulomb yield curve [*Ip et al.*, 1991].

[5] The MCE, teardrop, and lens yield curves were aimed at representing the homogeneous behavior of an ensemble of oriented ice leads or cracks that are often manifest as sharp discontinuities [*Stern et al.*, 1995]. Because they are isotropic, however, they can be as easily implemented in large-scale climate models as the widely used ellipse yield curve. How do they behave in large-scale climate models with a model resolution ranging from tens to hundreds of km

that cannot adequately resolve most of the oriented ice flaws? How does biaxial tension influence sea ice simulations in climate models? This paper aims to address these questions by comparing model performance of these various rheologies. We have developed mathematical formulations for teardrop and parabolic lens yield curves with and without biaxial tensile stress (Figure 1). These plastic yield curves, together with the MCE and ellipse curves, have been integrated in an arctic ice-ocean model to investigate the rheological effect. The ice-ocean model is briefly described in section 2. The rheologies are described in section 3. A detailed derivation of the teardrop and lens rheologies is presented in Appendix A. The derivation of the total normalized energy dissipation rate (see section 2) needed to determine ridging and lead opening is presented in Appendix B. Model behaviors of these rheologies are compared in section 4; the results are summarized in section 5.

## 2. Model Description

[6] The coupled ice-ocean model consists of two components: a 12-category thickness and enthalpy distribution sea ice model [*Zhang and Rothrock*, 2001] and an ocean model. The ocean model is based on the Bryan-Cox model [*Bryan*, 1969; *Cox*, 1984]. Detailed information about the ocean model is given by *Zhang et al.* [1998]. For reference, some aspects of the sea ice model are described in the following subsections. Additional ice model information is given by *Zhang and Rothrock* [2001].

### 2.1. Sea Ice Model

[7] The sea ice momentum balance follows *Hibler* [1979]:

$$m\partial\mathbf{u}/\partial t = -m\bar{f}\mathbf{k} \times \mathbf{u} + \tau_a + \tau_w - mg\nabla_H p(0) + \nabla \cdot \sigma, \quad (1)$$

where  $m$  is ice mass per unit area,  $\mathbf{u}$  is ice velocity,  $\bar{f}$  is the Coriolis parameter,  $\mathbf{k}$  is the unit vector in the  $z$  direction,  $\tau_a$  is air drag,  $\tau_w$  is water drag,  $g$  is the acceleration due to gravity,  $p(0)$  is sea surface dynamic height, and  $\sigma$  is ice internal stress tensor ( $\sigma_{ij}$ ). The last term in (1) represents an internal ice interaction force, with the stress tensor being related to ice strain rate and strength following the viscous-plastic constitutive law:

$$\sigma_{ij} = 2\eta\dot{\epsilon}_{ij} + (\zeta - \eta)\dot{\epsilon}_{kk}\delta_{ij} - (P/2)\delta_{ij}, \quad (2)$$

where  $\dot{\epsilon}_{ij}$  is the ice strain rate tensor,  $P$  is ice strength,  $\delta_{ij}$  is the Kronecker delta, and  $\zeta$  and  $\eta$  are the bulk and shear viscosities. The nonlinear viscosities are

$$\zeta = P/2\Delta \quad \text{and} \quad \eta = \zeta/e^2 \quad (3)$$

for the ellipse rheology and

$$\zeta = P/2\Delta; \quad \eta = (P/1.8 - \zeta\dot{\epsilon}_{kk})/(1.4\dot{s}) \quad (4)$$

for the MCE rheology [*Hibler and Schulson*, 2000]. In (3) and (4),  $\Delta = [(\dot{\epsilon}_{11}^2 + \dot{\epsilon}_{22}^2)(1 + e^{-2}) + 4e^{-2}\dot{\epsilon}_{12}^2 + 2\dot{\epsilon}_{11}\dot{\epsilon}_{22}(1 - e^{-2})]^{1/2}$  is a deformation function for the ellipse rheology,  $e = 2$  is the

ratio of principal axes of the ellipse,  $\dot{\epsilon}_{kk} = \dot{\epsilon}_{11} + \dot{\epsilon}_{22}$  is the divergence rate, and  $\dot{s} = [(\dot{\epsilon}_{11} - \dot{\epsilon}_{22})^2 + 4\dot{\epsilon}_{12}^2]^{1/2}$  is the maximum shear strain rate. The viscosities for teardrop and lens rheologies are derived in Appendix A. The ice momentum equation, with a viscous-plastic rheology and seasonally varying air drag coefficients and turning angles [Overland and Colony, 1994], is solved using the LSR ice dynamics solver [Zhang and Hibler, 1997].

[8] There are two conservation equations for thickness distributions of ridged ice and undeformed ice, respectively, which are written as [Flato and Hibler, 1995]:

$$\frac{\partial g_r}{\partial t} = -\nabla \cdot (\mathbf{u}g_r) - \frac{\partial(f_r g_r)}{\partial h} + \psi_r + F_r \quad (5)$$

$$\frac{\partial g_u}{\partial t} = -\nabla \cdot (\mathbf{u}g_u) - \frac{\partial(f_u g_u)}{\partial h} + \psi_u + F_u, \quad (6)$$

where the subscript  $r$  refers to ridged ice, the subscript  $u$  refers to undeformed ice,  $g_r(h)$  and  $g_u(h)$  are the ridged and undeformed ice thickness distributions, respectively,  $f_r$  and  $f_u$  are ice growth rates,  $\psi_r$  and  $\psi_u$  are the redistribution functions that describe the change in thickness distribution due to ridging, and  $F_r$  and  $F_u$  are lateral melting terms.

[9] The redistribution functions can be written as [Flato and Hibler, 1995]:

$$\psi_r = M \frac{-\alpha(h)g_r(h) + \int_0^\infty \beta(h', h)\alpha(h')g(h')dh'}{\int_0^\infty \left[ \alpha(h)g(h) - \int_0^\infty \beta(h', h)\alpha(h')g(h')dh' \right] dh}, \quad (7)$$

$$\psi_u = \delta(h)[M + \dot{\epsilon}_{kk}] + M \frac{-\alpha(h)g_u(h)}{\int_0^\infty \left[ \alpha(h)g(h) - \int_0^\infty \beta(h', h)\alpha(h')g(h')dh' \right] dh}, \quad (8)$$

where  $M$  is the normalized mechanical energy dissipation rate due to ridge creation,  $\delta(h)$  is the delta function,  $\alpha(h)$  is a function specifying which categories of ice participate in ridging, and  $\beta(h', h)$  is a redistributor of the thickness distribution. The normalized mechanical energy dissipation rate  $M$  is written as [Flato and Hibler, 1995]:

$$M = C_s \frac{1}{2} (\bar{\Delta} - |\dot{\epsilon}_{kk}|) - \min(\dot{\epsilon}_{kk}, 0), \quad (9)$$

where the generalized deformation function  $\bar{\Delta}$  is dependent on individual plastic yield curves and equals  $\Delta$  in (3) or (4) for the ellipse yield curve, and  $C_s$  is the shear ridging parameter that determines how much of the total mechanical energy dissipation rate is allocated for ridging (or how much of the shear deformation work goes into ridge building). The  $\bar{\Delta}$  function can be derived from the total normalized mechanical energy dissipation rate  $P^{-1}\sigma_{ij}\dot{\epsilon}_{ij}$  such that

$$P^{-1}\sigma_{ij}\dot{\epsilon}_{ij} = \frac{1}{2}(\bar{\Delta} - \dot{\epsilon}_{kk}). \quad (10)$$

We derive  $\bar{\Delta}$  and hence the normalized energy dissipation rate (9) in Appendix B for other yield curves under consideration. The shear ridging parameter and other parameters governing the ridging processes, such as the frictional dissipation coefficient and the ridge participation constant, are given by Flato and Hibler [1995] (see their Table 3 for the standard case).

[10] Although (5) and (6) are solved separately, they can be combined into one equation for analyzing model results, such that

$$\frac{\partial g}{\partial t} = -\nabla \cdot (\mathbf{u}g) - \frac{\partial(fg)}{\partial h} + \psi + F, \quad (11)$$

where  $g(h) = g_r(h) + g_u(h)$  is the (total) ice thickness distribution that is a normalized probability function [Thorndike et al., 1975; Hibler, 1980],  $f(h) = f_r(h) + f_u(h)$  is ice growth rate,  $\psi = \psi_r + \psi_u$  is the total redistribution function due to ridging, and  $F_L = F_r + F_u$  is the total lateral melting. Note that (total) ice thickness is the summation of ridged ice thickness and undeformed ice thickness. By ridged ice thickness, we mean ridged ice volume per unit area; likewise for undeformed ice thickness.

## 2.2. Numerical Framework and Surface Forcing

[11] The model domain covers the Arctic, Barents, and GIN (Greenland-Iceland-Norwegian) seas. It has a horizontal resolution of 40 km  $\times$  40 km, 21 ocean levels, and 12 thickness categories each for undeformed ice, ridged ice, ice enthalpy, and snow. The partition of ice thickness categories is given by Zhang et al. [2000].

[12] Daily surface atmospheric forcing for six years 1992–1997 was used to drive the model. The forcing consists of geostrophic winds, surface air temperature, specific humidity, and downward longwave and shortwave radiative fluxes. (The forcing can be downloaded from the POLES Sea Ice Model Forcing Data Set Web site at [http://psc.apl.washington.edu/POLES/model\\_forcings/ModelForcings.html](http://psc.apl.washington.edu/POLES/model_forcings/ModelForcings.html)). The geostrophic winds are calculated using the sea level pressure (SLP) fields from the International Arctic Buoy Program (IABP) [see Colony and Rigor, 1993]. The 2-m surface air temperature data are derived from buoys, manned drifting stations, and land stations [Rigor et al., 2000]. The specific humidity and downward longwave and shortwave radiative fluxes are calculated following the method of Parkinson and Washington [1979] based on the SLP and air temperature fields. Model input also includes river runoff and precipitation as detailed by Hibler and Bryan [1987] and Zhang et al. [1998].

## 3. Rheology Description

[13] We examine mainly six rheologies, four with and two without tensile stress (Figure 1). They are denoted throughout the paper as ellipse, MCE, teardrop, lens, teardrop 1, and lens 1. The main features of each rheology are summarized as follows.

[14] Ellipse [Hibler, 1979] allows tensile stress but does not permit biaxial tensile stress; obeys the normal flow rule; taken as the standard yield curve because of its wide use. MCE [Hibler and Schulson, 2000] allows biaxial tensile stress; obeys the normal flow rule along the elliptical part of

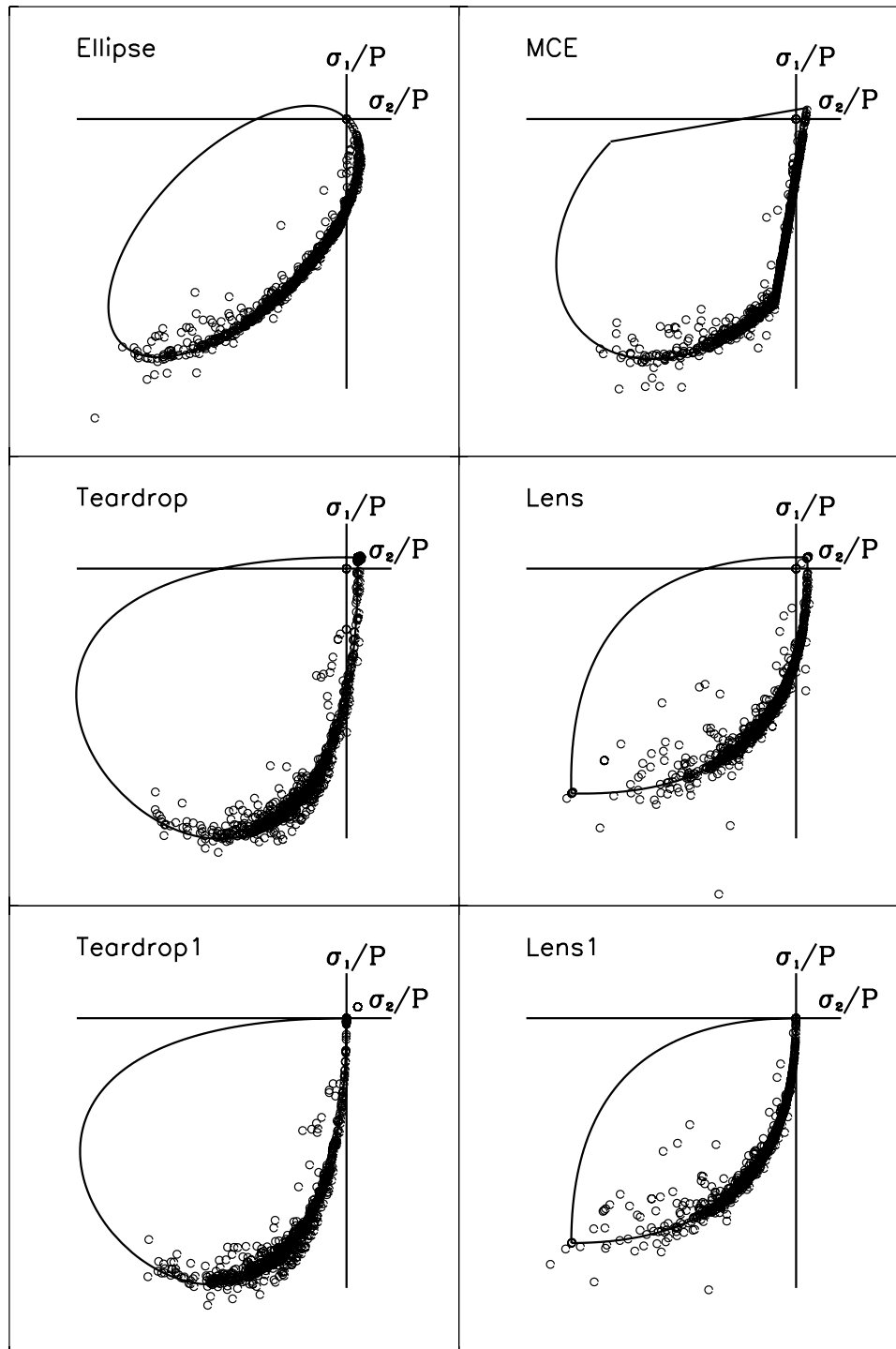


**Figure 2.** Normalized principal ice internal stresses for the first day of 1993. The stress at every model cell with ice is plotted.

the yield curve and is based on Coulombic friction failure elsewhere. Teardrop (section A1) allows biaxial tensile stress; obeys the normal flow rule; has the largest aspect ratio or “fatness” among the rheologies under consideration. Lens (section A2) allows biaxial and uniaxial tensile stress; obeys the normal flow rule; has about the same aspect ratio as ellipse. Teardrop 1 is the same as teardrop except that it does not allow tensile stress. Lens 1 is the same as lens except that it does not allow tensile stress.

[15] The maximum allowable biaxial tensile stress for teardrop and lens is set to be about the same as that for MCE (see Appendix A), and is about the same as the uniaxial tensile stress for ellipse (Figure 1). Also note that all the rheologies except MCE allow a maximum compressive stress to be equal to the ice strength. As a result, teardrop and lens are slightly fatter or allow higher maximum shear stress than teardrop 1 and lens 1, respectively.

**Table 1.** Frequency in Percent of Daily Stresses in Each State, Biaxial Tensile, Mixed Tensile/Compressive, and Biaxial Compressive, Calculated for All Ice Points Over 1993–1997

Case	Biaxial Tensile Stress State	Tensile/Compressive Stress State	Biaxial Compressive Stress State
Ellipse	–	21	79
MCE	1	11	88
Teardrop	7	9	84
Lens	4	11	85
Teardrop 1	–	–	100
Lens 1	–	–	100

[16] We focus on the above six rheologies. However, we have implemented and examined an additional set of teardrop and lens rheologies in order to single out the effect of biaxial tensile stress. They are described as follows.

[17] Teardrop 2 has the same maximum biaxial tensile stress as and a smaller maximum compressive stress than teardrop; has the same shape and fatness as teardrop 1 (Appendix A); allows about the same maximum compressive stress as MCE. Lens 2 has the same maximum biaxial tensile stress as and a smaller maximum compressive stress than lens, has the same shape and fatness as lens 1, and allows about the same maximum compressive stress as MCE.

#### 4. Simulation Results

[18] To examine the effect of sea ice rheology in numerical investigations of climate, we conducted a model run using each of the eight rheologies mentioned above. These runs were carried out for the 6-year period 1992–1997 using the same initial conditions obtained by running the standard ellipse case from 1979 to 1991. 1992 was taken as a year of transition after which the influence of the 1991 conditions on the results of later years is found to be minimal. The results for 1993–1997 were compared among model runs, and to buoy motion data and to submarine ice draft data.

##### 4.1. Ice Stress and Deformation

[19] Internal ice stress in principal stress space was normalized by ice strength (Figure 2). The ice simulated by each of the six models is in a reasonably good state of viscous-plastic flow: the majority of the stresses lie on the yield curve (plastic flow) and most of the remaining stresses fall inside the yield curve (viscous flow). About 10% of stresses fall outside the yield curve, which do not follow the true viscous-plastic rheology because of numerical inaccuracy.

[20] We considered three states of the simulated stresses: biaxial tensile ( $\sigma_1 > 0, \sigma_2 > 0$ ), biaxial compressive ( $\sigma_1 \leq 0, \sigma_2 \leq 0$ ), and mixed tensile/compressive ( $\sigma_1\sigma_2 \leq 0$ ) states. The frequency of these three states is given in Table 1. Of all cases, ellipse has the fewest biaxial compressive stresses and the most mixed tensile/compressive stresses, while teardrop possesses the most biaxial tensile stresses and the fewest mixed stresses. The MCE has only 1 percent biaxial tensile stresses.

[21] We also calculated the frequency of three strain rate states: biaxial extension ( $\dot{\epsilon}_1 > 0, \dot{\epsilon}_2 > 0$ ), biaxial compression

( $\dot{\epsilon}_1 \leq 0, \dot{\epsilon}_2 \leq 0$ ), and mixed extension/compression ( $\dot{\epsilon}_1\dot{\epsilon}_2 \leq 0$ ). The strain rate frequencies do not differ significantly among the various rheologies (Table 2). They all occupy mostly mixed extension/compression states. They also occupy more biaxial extension (divergence) states than biaxial compression (convergence) states. The teardrop rheologies have slightly more biaxial extension and biaxial compression than other rheologies. The strain rate frequencies created by the lens and ellipse rheologies are almost identical. This may be due to the fact that they obey the normal flow rule and have similar fatness. Note also that incorporating biaxial tensile stress does not change the frequencies.

[22] Figure 3a compares the distributions of shear stress  $[(\sigma_{11} - \sigma_{22})^2 + 4\sigma_{12}^2]^{1/2}$  calculated for the whole period of 1993–1997. For all the rheologies that fully obey the normal flow rule, the stress distribution exhibits a two-peak system; the first peak is around zero stress, and the second peak is around  $16,000 \text{ N m}^{-1}$  for ellipse and the two lens rheologies and  $30,000 \text{ N m}^{-1}$  for the two teardrop rheologies. The teardrop rheologies are relatively fat and create more large shear stresses than the other rheologies. Teardrop and lens create more large shear stresses than teardrop 1 and lens 1, respectively. This is because their plastic yield curves are slightly fatter than their counterparts (Figure 1). The unique case is MCE, which does not generate a second peak at all. This is because MCE usually does not tend to create a second peak in spring and fall while other cases do (Figures 4b and 4d). It does create a peak around  $23,000 \text{ N m}^{-1}$  in winter, but the peak is not as prominent as those created by other rheologies (Figure 4a). This may be due to its friction-based failure along the Mohr-Coulomb part of the yield curve where the normal flow rule does not apply. In summer these rheologies all have a similar distribution of shear stress with a large fraction of zero shear stress (Figure 4c). Note also that teardrop and lens rheologies have a higher fraction of zero stress than MCE and ellipse in winter, and teardrop rheologies have a third peak around  $6000 \text{ N m}^{-1}$  in fall.

[23] The comparison of the shear deformation ( $\dot{\gamma}$ ) distributions (Figure 3b) appears to be more straightforward than that of the shear stress distributions. By creating larger shear stress, a fatter yield curve is likely to result in more small shear deformations and fewer large ones. The rheologies all create about same percentage of  $0.5\% \text{ d}^{-1}$  shear deformation.

##### 4.2. Ice Motion

[24] The 1993–1997 mean fields of modeled ice velocity and velocity difference between various rheologies are

**Table 2.** Frequency in Percent of Daily Strain Rates for 1993–1997 in Each State, Biaxial Extension, Mixed Extension/Compression, and Biaxial Compression

Case	Biaxial Extension	Extension/Compression	Biaxial Compression
Ellipse	5	92	3
MCE	5	91	4
Teardrop	7	88	5
Lens	5	92	3
Teardrop 1	7	88	5
Lens 1	5	92	3

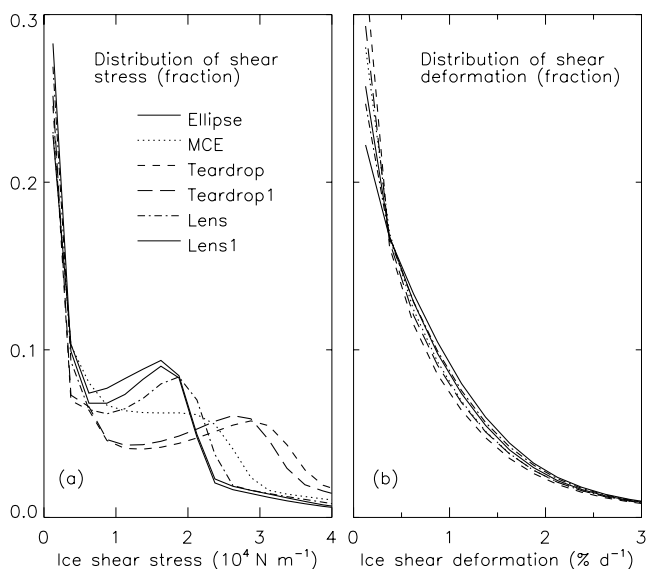


**Figure 3.** Distributions of simulated (a) shear stress and (b) shear deformation calculated from daily model results during 1993–1997.

shown in Figure 5. In agreement with buoy observations [Rigor *et al.*, 2002], the mean spatial pattern of arctic ice motion consists of a Beaufort Gyre, a Transpolar Drift Stream, and an East Greenland Current (Figure 5a). The velocities for MCE and especially teardrop are smaller than those for ellipse (Figures 5b and 5c). This reduced motion is due to MCE and teardrop being fatter than the ellipse, which results in higher shear stresses (Figure 3a) and lower ice speeds. One of the consequences is a reduced shear deformation (Figure 3b). Another is a reduced ice export at Fram Strait (Figures 5b and 5c). On the other hand, the velocities for lens and ellipse are very similar (Figure 5d), which may have something to do with their similar fatness and inclusion of tensile stress. Incorporating biaxial tensile stress while reducing the maximum compressive stress tends to slightly reduce ice velocity (Figures 5g and 5h); incorporating biaxial tensile stress while allowing the same maximum compressive stress (equal to ice strength) tends to further reduce ice velocity (Figures 5e and 5f), owing to its tendency to create a higher shear stress (Figure 3a).

[25] The magnitude of the simulated ice velocities from each rheology run is also reflected in a comparison with buoy velocities that are provided by IABP [Colony and Rigor, 1993]. Given the dynamical and thermodynamical forcing and Overland and Colony's [1994] seasonal air drag coefficients and turning angles, the daily mean ice speed calculated by all but the two lens rheologies is slower, to a varying degree, than the daily mean buoy speed (Table 3). Among all the rheologies, the teardrop 5-day and 10-day mean speeds are the closest to the corresponding buoy speeds, but its bias in daily mean speed is the largest. The difference in daily mean speed between lens 1 and teardrop is  $1.1 \text{ cm s}^{-1}$ , or 15%. Note that the magnitude of ice velocity simulated by most of the rheology cases is smaller than that of buoy velocity on a 1-day timescale, and greater on a longer timescale. This may indicate a model deficiency in capturing actual ice motion variability on various time-

scales. However, model-data correlation is improved on a longer timescale (Table 3).

### 4.3. Ice Thickness

[26] Figure 6a shows annual cycles of ice thickness averaged over the Arctic Basin. The 1993–1997 mean ice thickness from MCE is noticeably larger than those from other cases. This is because MCE has significantly more ridged ice (Figure 6b), while the reduction in undeformed ice is relatively small in comparison with ellipse (Figure 6c). The ice thickness for teardrop is only slightly larger than that for ellipse because the increase in ridged ice thickness is smaller than for MCE. Teardrop 1 and the two lens rheology cases, on the other hand, produce less ice than ellipse; these cases produce a relatively large reduction in undeformed ice.

[27] The mean and difference fields of ice thickness are plotted in Figure 7. The pattern of the thickness field simulated with ellipse (Figure 7a) agrees reasonably well with that observed by Bourke and McLaren [1992]. This is a pattern of thicker ice off the Canadian Archipelago and north Greenland coast and thinner ice in the eastern Arctic. Compared to ellipse, MCE (Figure 7b) causes ice thickness to increase considerably over most of the Arctic Basin, up to 0.6 m. The increase in ice thickness caused by teardrop is more limited to the Eurasian Basin, Laptev and Kara seas, and the area a certain distance away from the Canadian Archipelago; it results in less ice in most of the Chukchi and Beaufort seas (Figure 7c). Particularly, ice is reduced along the Alaskan and Canadian Archipelago coasts. This is a significant spatial redistribution of ice mass, relative to

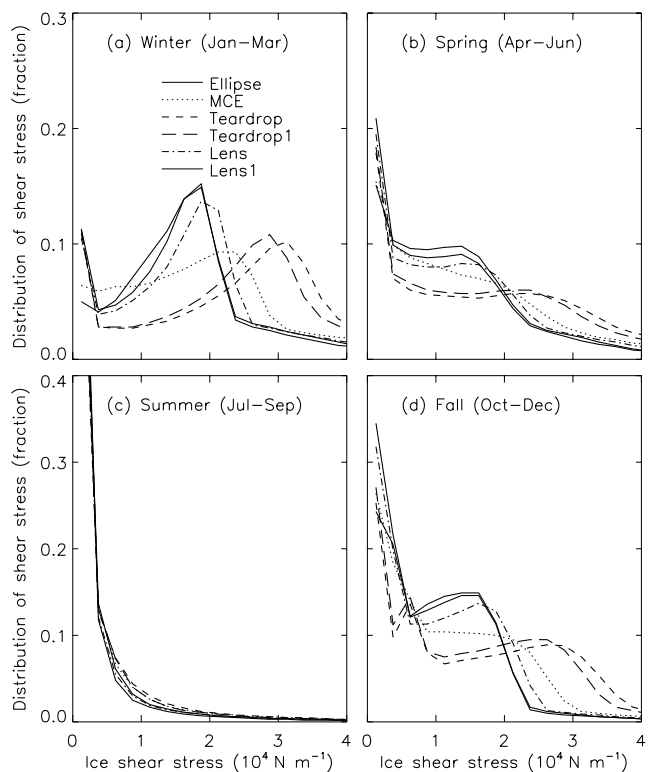


**Figure 4.** Seasonal distributions of simulated shear stress calculated from daily model results during 1993–1997.

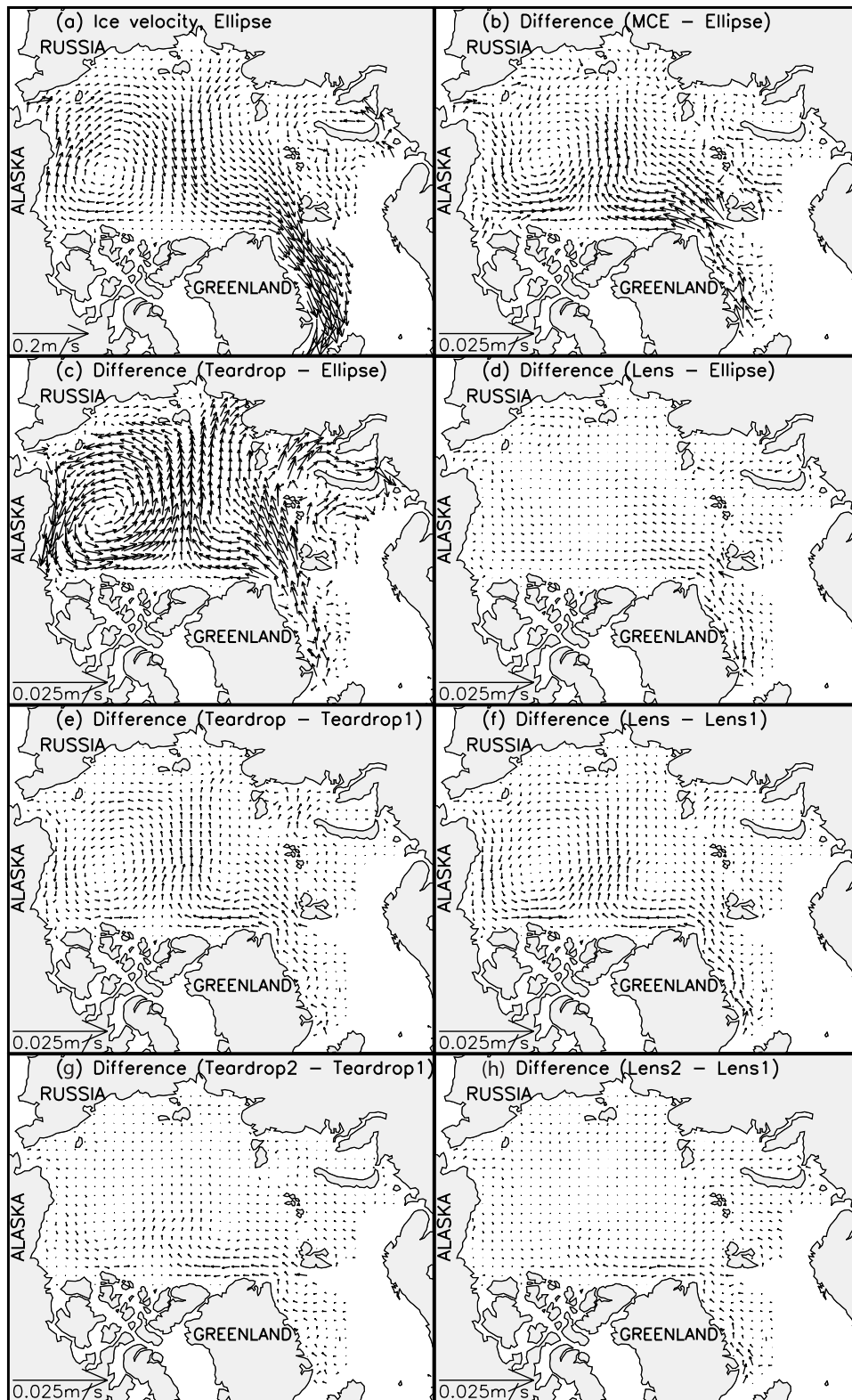


**Figure 5.** The 1993–1997 (a) mean ice velocity and (b–h) difference fields. One vector is drawn for every nine grid cells. Note the different vector scales in different panels.

ellipse. Lens, on the other hand, creates a bit more ice off the Canadian Archipelago and north Greenland coast and a bit less ice over other areas (Figure 7d). The thickness difference in the GIN Sea is closely linked to the effect on

ice export at Fram Strait. In addition, allowing biaxial tensile stress tends to increase ice thickness over most of the Arctic Basin (Figures 7e–7h). The basic features of the thickness difference fields in Figures 7e and 7f are similar to

**Table 3.** Comparisons of Model and Buoy Velocities Based on Daily, 5-day, and 10-day Averages<sup>a</sup>

Case	Mean Model Ice Speed, cm s <sup>-1</sup>	Model Bias <sup>b</sup>	Error SD <sup>c</sup>	Correlation, %
Ellipse	7.8 (6.9) [6.1]	-0.1 (0.6) [0.8]	7.1 (5.0) [4.0]	73 (80) [83]
MCE	7.4 (6.5) [5.8]	-0.5 (0.2) [0.5]	7.0 (4.9) [3.9]	73 (80) [83]
Teardrop	7.1 (6.2) [5.4]	-0.8 (-0.1) [0.1]	7.0 (4.9) [3.8]	72 (79) [82]
Lens	7.9 (6.9) [6.0]	-0.0 (0.6) [0.7]	7.0 (5.0) [3.9]	74 (81) [83]
Teardrop 1	7.4 (6.5) [5.7]	-0.5 (0.2) [0.4]	7.0 (4.9) [3.8]	73 (80) [83]
Lens 1	8.2 (7.2) [6.2]	0.3 (0.9) [0.9]	7.0 (5.0) [4.0]	75 (81) [84]

<sup>a</sup>The 5-day averages are given in parentheses, and the 10-day averages are given in brackets.

<sup>b</sup>During 1993–1997, there are 38,466 daily mean buoy velocities with a mean speed of 7.9 cm s<sup>-1</sup>, 7348 5-day mean buoy velocities with a mean speed of 6.3 cm s<sup>-1</sup>, and 3616 10-day mean buoy velocities with a mean speed of 5.3 cm s<sup>-1</sup>.

<sup>c</sup>SD is standard deviation.

those in Figures 7g and 7h. This indicates that the incorporation of biaxial tensile stress is more influential on ice thickness than allowing the maximum compressive stress to be equal to ice strength thus slightly increasing the fatness of the yield curve (Figures A1 and A2).

[28] What causes the differences in the spatial distribution of ice mass? Ridged ice production contributes to some of the differences (Figure 8). The mean ridged ice production field simulated by ellipse displays more ridging in the western Arctic than in the eastern Arctic (Figure 8a). Because MCE and teardrop are fatter than ellipse, they increase ridged ice production over most of the Arctic Basin (Figures 8b and 8c). The largest increase in either case is in an area about 1500 km off the Canadian coast, where the increase in ice thickness is the largest (Figures 7b and 7c). Note that MCE is less fat than teardrop, but it creates more ridging than teardrop over a large area of the Arctic Basin. This may be due to the fact that MCE does not fully follow the normal flow rule and its maximum compressive stress is less than ice strength. Note also that MCE reduces ridged ice production off the Canadian and North Greenland coast, whereas teardrop reduces ridging along almost all the Arctic coast. One explanation is that a large shear stress from teardrop or MCE is more likely associated with a large compressive stress than other rheologies (Figure 2). Such behavior is likely to cause teardrop and, to a lesser degree, MCE to create strong shear stress in the coastal convergence zones, leading to a weakened shear deformation (Figure 3) and therefore a reduced ridged ice production.

[29] Lens only slightly increases ridged ice production (Figure 8d), which is why it has slightly more ridged ice than ellipse (Figure 6b). Incorporating tensile stress reduces ridged ice production along the Canadian coast and increases the production in the central Arctic. This effect is reflected in the differences between the two teardrop cases and between the two lens cases (not shown).

[30] Ice export at Fram Strait is an important sink in the arctic ice mass budget. In units of 10<sup>12</sup> m<sup>3</sup> yr<sup>-1</sup>, the 1993–1997 mean export at Fram Strait is 3.16 for ellipse, 3.04 for MCE, 2.99 for teardrop, and 3.05 for lens, which gives a difference range of about 6%. Lens produces less export than ellipse because of a thinner ice cover in the Arctic Basin (Figure 7d), indicating ice thickness in the Fram Strait area is a dominating factor in ice export; MCE and teardrop produce less export because of reduced ice velocity at Fram Strait (Figures 5b and 5c), indicating ice speed at Fram

Strait is a dominating factor. When the reduction in export is due to reduced velocity at Fram Strait, the result is a thicker ice cover in the Arctic Basin. The incorporation of biaxial tensile stress, by allowing the yield curve to enter the first quadrant of the stress space, also leads to a reduction in export, but to a lesser degree (Figures 5e–5h).

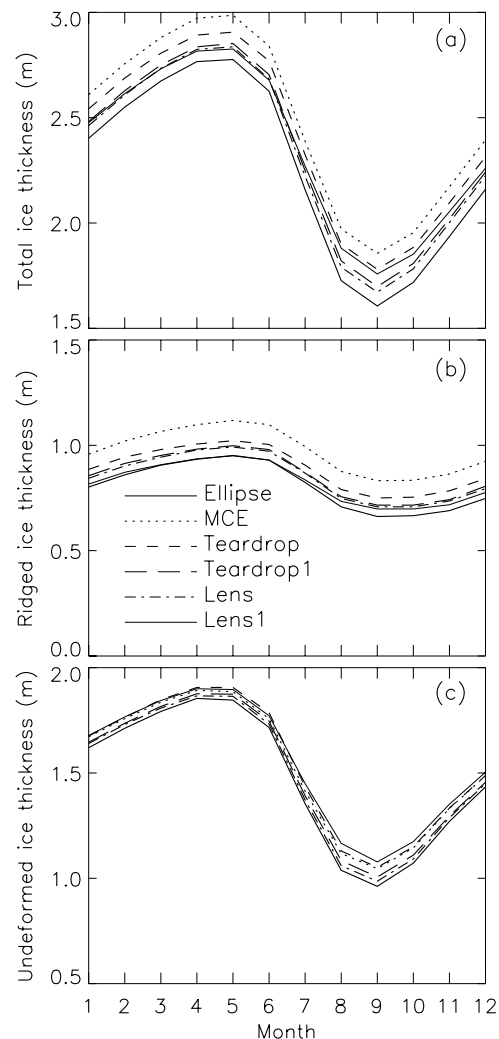


**Figure 6.** The 1993–1997 mean annual cycles of (a) (total) ice thickness, (b) ridged ice thickness, and (c) undeformed ice thickness. Thickness is defined as volume per unit area.

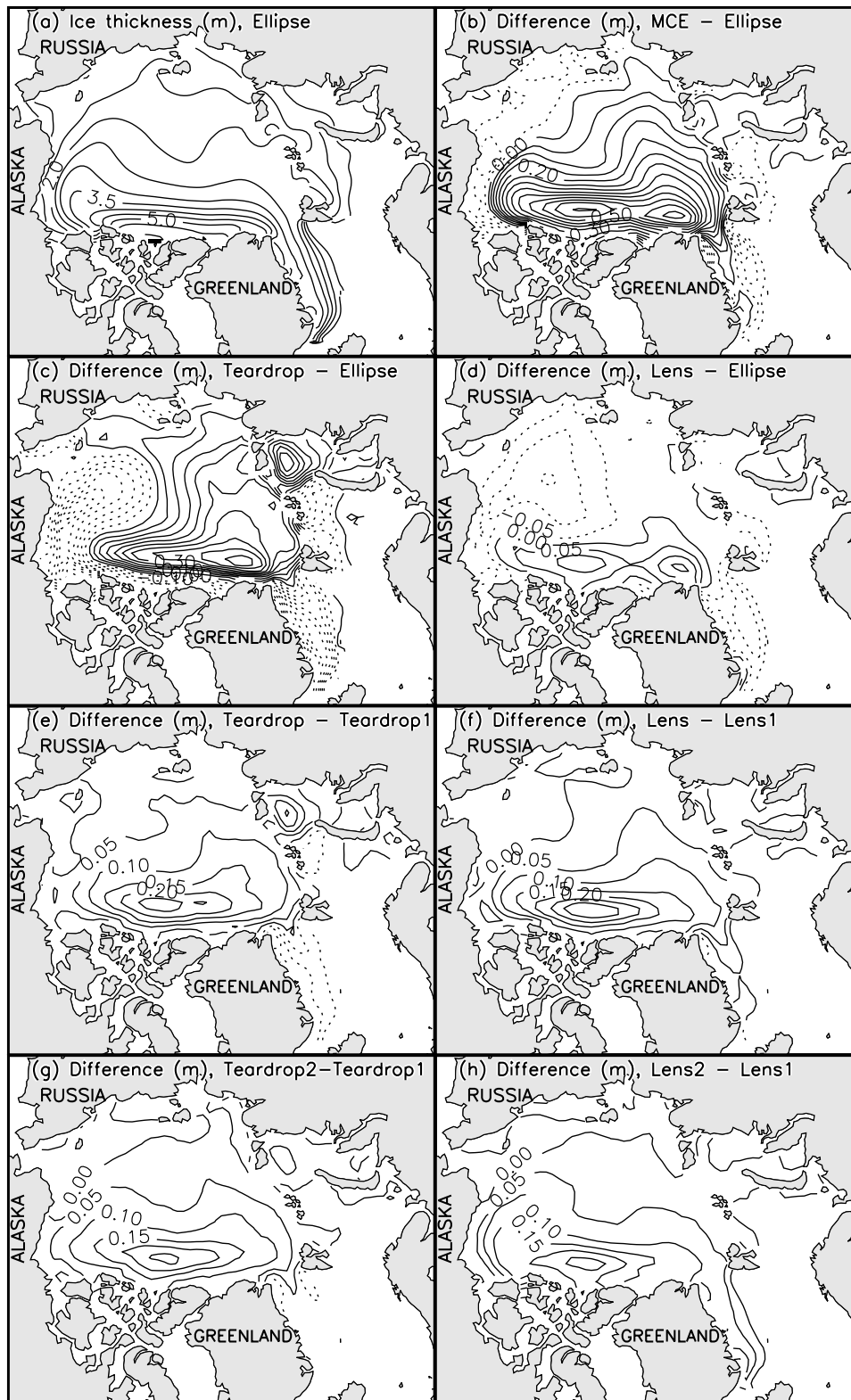


**Figure 7.** The 1993–1997 (a) mean ice thickness and (b–h) difference fields. The contour interval is 0.5 m for the mean field and 0.05 m for the difference fields.

#### 4.4. Comparison With Submarine Ice Draft

[31] We compared the model ice draft (simulated ice thickness multiplied by 0.89) with submarine observations of ice draft. The observations, with an uncertainty of about

0.15 m, were acquired by four submarine cruises from 1993 to 1997 (Figure 9). They were compared with model drafts sampled at the location of each dot at the corresponding time (Table 4 and Figure 9). Given the dynamical and

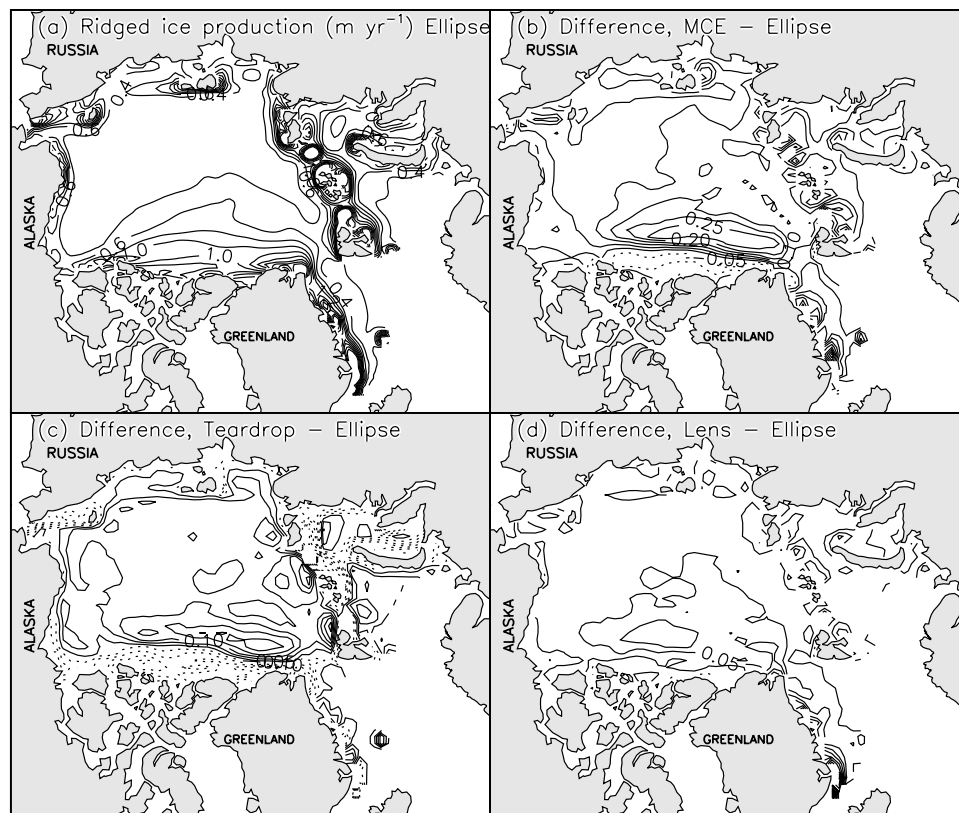


**Figure 8.** The 1993–1997 (a) mean ridged ice production and (b–d) difference fields. The contour interval is  $0.2 \text{ m yr}^{-1}$  for the mean field and  $0.05 \text{ m yr}^{-1}$  for the difference fields.

thermodynamical forcing and model parameterization, MCE and lens 1 have relatively higher bias in mean ice draft along the submarine tracks. The difference in the draft between MCE and the lens 1 is  $0.30 \text{ m}$ , or 16%. The lens rheologies generally perform worse than the teardrop rheologies. Lens 1, in particular, has relatively low correlation and high bias and error standard deviation (SD).

[32] Moderately, teardrop appears to have the best overall performance in obtaining the highest correlation and the lowest bias and error SD. This indicates that the spatial difference in ice mass as seen in Figure 7c helps improve model agreement with observations. As shown in Figure 9a, ellipse tends to overestimate ice draft in the Beaufort Sea and underestimate ice draft in the Eurasian Basin and near the North Pole for 1993–1997. A careful examination reveals that, to a varying degree, teardrop tends to reduce such model bias in all these areas (Figures 9c and 10). MCE is also able to somewhat reduce model bias in the Eurasian Basin and North Pole area, but not in the Beaufort Sea. In addition, it tends to create more large overestimates than other rheologies (Figure 10). In comparison with ellipse, the two lens rheologies actually enlarge the spatial model bias slightly (Figure 9d). It consistently underestimates ice draft such that its distribution of model-data difference in ice draft peaks at  $-0.6 \text{ m}$  (Figure 10).

#### 4.5. Surface Energy Exchanges

[33] To what degree does sea ice rheology affect the surface energy exchange in climate models? To address this question, we plotted the 1993–1997 mean and difference

fields of upward net surface heat flux (Figure 11). The differences in the surface heat loss are generally less than  $0.5 \text{ W m}^{-2}$  in the central Arctic. The differences in the averaged values over the entire ice covered areas are also within  $0.5 \text{ W m}^{-2}$ , with the average being  $9.2 \text{ W m}^{-2}$  for ellipse, teardrop, and lens, and  $9.6 \text{ W m}^{-2}$  for MCE. However, locally differences can reach  $3 \text{ W m}^{-2}$  in the Arctic marginal seas, such as the East Siberian and Laptev seas, and in some coastal areas. Outside the Arctic Basin, mainly in the marginal ice zones in the Barents and GIN seas, the differences are much larger, up to  $8 \text{ W m}^{-2}$  (Figures 11 and 12), owing to differences in surface conditions such as ice coverage and thickness. The average surface heat loss over areas covered by ice thinner than  $1 \text{ m}$  is  $32 \text{ W m}^{-2}$  for ellipse and teardrop,  $34 \text{ W m}^{-2}$  for MCE, and  $33 \text{ W m}^{-2}$  for lens. That is, the difference between MCE and ellipse is 6%. In addition, the areas with a difference of  $3 \text{ W m}^{-2}$  or more consist of up to 10% of the entire ice covered areas and 27% of the areas covered by ice thinner than  $1 \text{ m}$  (Figure 12). This is also true for the components of the surface heat flux: net shortwave and longwave radiative fluxes and net sensible and latent heat fluxes (not shown). This indicates that sea ice rheology, by changing ice motion, deformation, and thickness, has a significant impact on the calculation of the surface energy budget, particularly in long-term modeling of climate change.

#### 5. Concluding Remarks

[34] We have developed mathematical formulations for sea ice constitutive laws that employ teardrop and parabolic lens plastic yield curves. Like the widely used ellipse

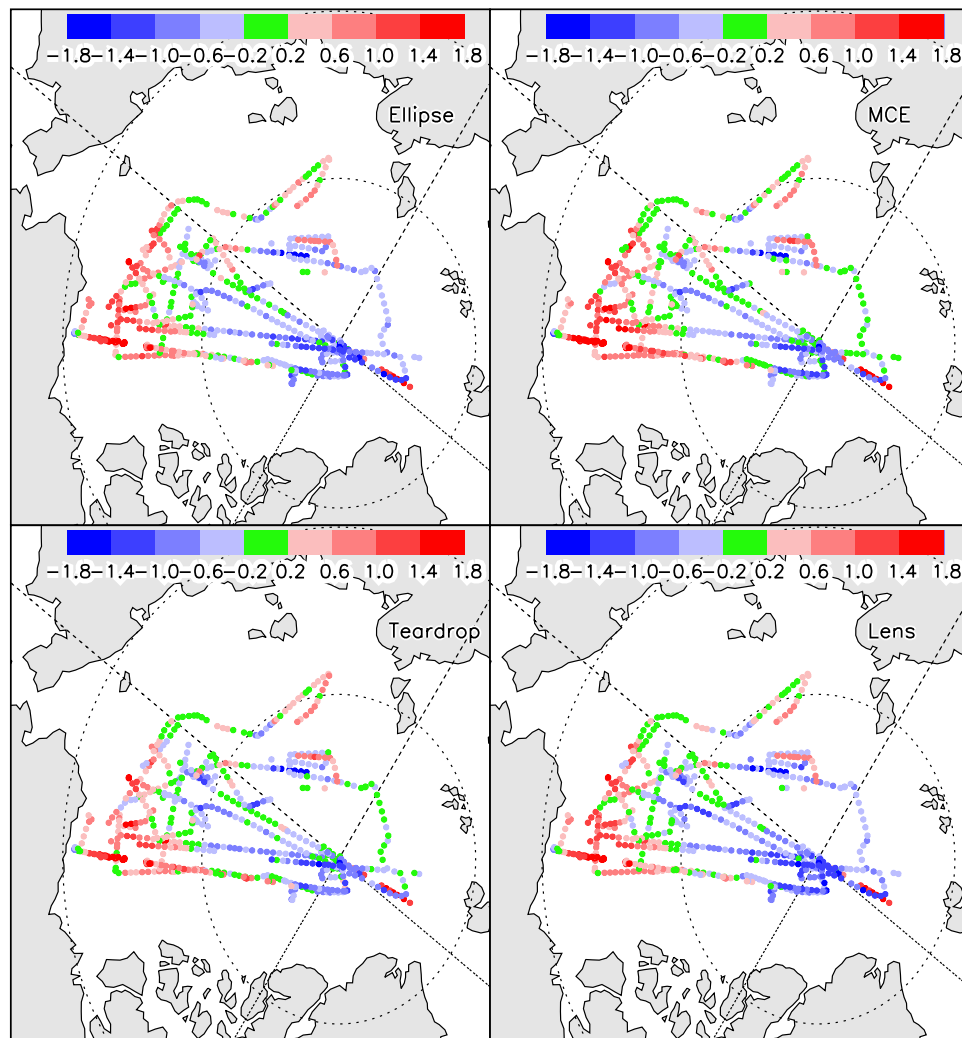


**Figure 9.** Modeled minus observed ice draft (m) along submarine cruise tracks from 1993 to 1997. Dots illustrate available observations of ice draft collected along four tracks of submarine cruises in September 1993, April 1994, September 1996, and September–October 1997. Each dot in the plot represents a record of ice thickness averaged over a distance of  $\sim 10$ – $50$  km along the tracks.

rheology [Hibler, 1979], they are isotropic plastic rheologies that obey the normal flow rule when ice fails; like the MCE rheology [Hibler and Schulson, 2000], they follow the laboratory observations of ice mechanical property by allowing varying amount of biaxial tensile stress. In order to examine the effects of a plastic rheology in numerical investigations of climate, the teardrop and lens rheologies, together with the ellipse and the MCE rheologies, were numerically implemented in a thickness and enthalpy distribution ice model for the Arctic, Barents, and GIN seas. Reasonably good viscous-plastic solutions are achieved using each rheology, with about 90% of ice internal stresses falling either on or inside the yield curves (Figure 2).

[35] Model results from a series of integrations indicate that plastic rheology has a significant effect on large-scale sea ice simulations. For the whole simulation period of 1993–1997, rheologies that fully follow the normal flow rule have shear stress distributions with two peaks, one at the zero shear stress and the second between  $16,000$ – $30,000$   $\text{N m}^{-1}$ . The second peak is around  $16,000$   $\text{N m}^{-1}$

for the ellipse and two lens rheologies and around  $30,000$   $\text{N m}^{-1}$  for the two teardrop rheologies. On the basis of Coulombic friction failure and only partially obeying the normal flow rule, the MCE rheology creates a shear stress distribution without a second peak. This is because MCE usually does not tend to create a second peak in spring and fall, an interesting distinction revealed by model results.

**Table 4.** Modeled and Observed Ice Drafts Compared Along Tracks of Four Submarine Cruises in 1993–1997<sup>a</sup>

Case	Mean Model Draft, m	Bias	Error SD	Correlation
Ellipse	2.01	0.04	0.71	0.44
MCE	2.13	0.16	0.75	0.47
Teardrop	2.01	0.04	0.69	0.51
Lens	1.91	−0.06	0.73	0.45
Teardrop 1	1.90	−0.07	0.69	0.50
Lens 1	1.83	−0.14	0.74	0.42

<sup>a</sup>There are 639 observed drafts with a mean of  $1.97$  m.

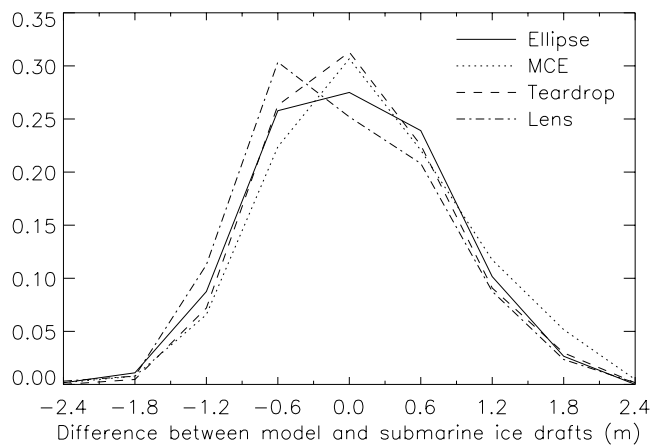


**Figure 10.** Distributions (fraction) of the difference between model and submarine ice drafts.

[36] The incorporation of biaxial tensile stress is likely to increase ice thickness in most of the Arctic Basin. Allowing biaxial tensile stress tends to affect the spatial distribution of ice thickness more strongly than allowing the maximum compressive stress to be the same as the ice strength (i.e., slightly increasing the fatness of the yield curve).

[37] A fatter yield curve tends to create a greater incidence of large shear stress values. Large shear stress tends

to reduce ice speed [Ip *et al.*, 1991], leading to a decrease in all components of ice circulation: the Beaufort Gyre, the Transpolar Drift Stream, the East Greenland Current, and the ice export at Fram Strait (Figure 5). This, in conjunction with the inclusion of biaxial tensile stress, leads to a substantial change in spatial distribution of ice mass. In addition, a fatter yield curve with biaxial tensile stress tends to create more ice ridging over most of the Arctic Basin, particularly in the area about 1500 km off the Canadian Archipelago. Consequently, teardrop yields thicker ice than ellipse in the Eurasian Basin, Laptev and Kara seas, and the area 1500 km off the Canadian coast, and thinner ice in most of the Chukchi and Beaufort seas (Figure 7c). MCE creates even thicker ice over a larger area of the Arctic (Figure 7b) even though MCE is not as fat as teardrop. This may be attributed to the fact that MCE partially follows the Coulombic friction failure and has a maximum compressive stress less than ice strength. The ellipse and lens yield curves are thinner and they create a thinner arctic ice cover than MCE and the two teardrop rheologies. The range in mean model ice draft along the four tracks of submarine cruises in 1993–1997 is 0.30 m or 16%.

[38] Given the dynamical and thermodynamical forcing, teardrop agrees moderately better with the submarine observations of ice draft than others in obtaining relatively high correlation and low bias and error SD. This is because teardrop tends to reduce, to a varying degree, spatial bias of modeled ice draft against the observations over most of the

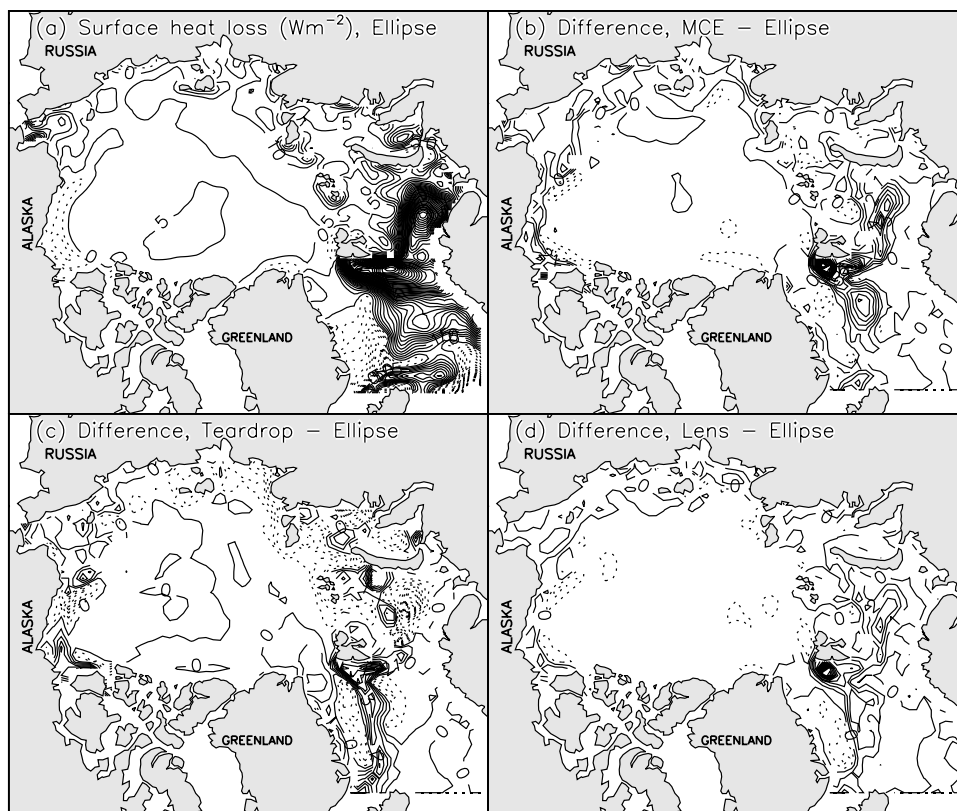


**Figure 11.** The 1993–1997 (a) mean net upward surface heat flux and (b–d) difference fields. The heat flux is the summation of longwave and shortwave radiations and sensible and latent heat fluxes. The contour interval is  $5 \text{ W m}^{-1}$  for the mean field and  $1 \text{ W m}^{-1}$  for the difference fields.

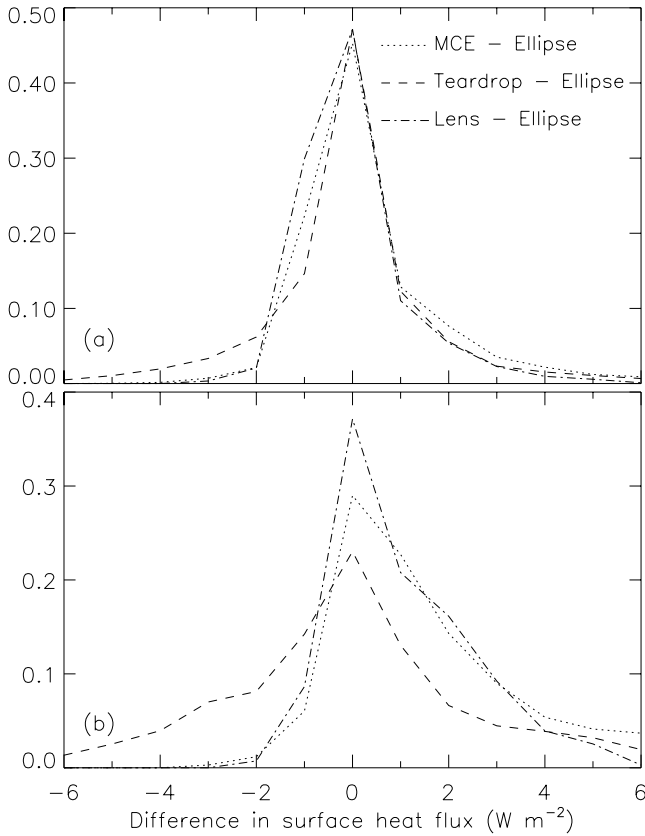


**Figure 12.** Distributions (fraction) of the difference in net surface heat flux for 1993–1997 (a) over ice-covered areas and (b) over areas covered by ice thinner than 1 m.

areas covered by 1993–1997 submarine cruises. Teardrop is also found to reduce ice thickness along the coastal convergence/shear zones, which contributes to the reduction of model bias in the Beaufort Sea.

[39] The results also indicate that plastic rheology, which changes the model's solution of ice motion, deformation, and thickness, has a significant impact on the computation of surface energy exchanges. Although the local differences in surface heat fluxes among all the rheology cases are generally less than  $0.5 \text{ W m}^{-2}$  in the central Arctic, they can be as high as  $3 \text{ W m}^{-2}$  in the Arctic marginal seas and as high as  $8 \text{ W m}^{-2}$  in the marginal ice zones in the Barents and GIN seas. Among the thin ice areas where greater surface exchanges occur, the percentage of the areas with a difference of  $3 \text{ W m}^{-2}$  or more can reach 27%. In a coupled climate model with atmosphere, ocean, and sea ice components, such differences would likely have a significant impact on the overall energy budget of the model.

[40] A variety of rheologies have been compared; all are isotropic rheologies that can be integrated easily in climate models. Although varying in performance, they all simulate reasonably realistic ice motion and thickness compared with buoy and submarine observations. These rheologies open up another dimension for model calibration and adjustment, in addition to traditional tuning of some model parameters such as air drag and ice strength. What rheology should we choose for climate modeling? The ellipse has been widely used and resulted in realistic results, but the MCE, teardrop,

and lens are all equipped with biaxial tensile stress that is in line with lab experiments. Teardrop is generally preferred because of its improved agreement with ice draft observations. However, this assessment is based on only one study. Whether teardrop is better in other applications needs to be examined.

## Appendix A: Derivation of Constitutive Laws With Teardrop and Lens Yield Curves

[41] In a normalized stress space (Figure A1), both teardrop and lens plastic yield curves can be described by a common equation

$$\sigma_{II}/P = -(\sigma_I/P - a)[1 + a + (\sigma_I/P - a)]^q, \quad (\text{A1})$$

where  $a$  is the biaxial tensile stress parameter,  $q$  is the fatness factor determining the shape of the curve ( $q = 1/2$  for teardrop and  $q = 1$  for parabolic lens), and  $\sigma_I$  and  $\sigma_{II}$  are defined as

$$\sigma_I = \frac{1}{2}(\sigma_1 + \sigma_2) \quad \text{and} \quad \sigma_{II} = \frac{1}{2}(\sigma_1 - \sigma_2), \quad (\text{A2})$$

where  $\sigma_1$  and  $\sigma_2$  are the principal stresses. If  $\dot{\epsilon}_I$  and  $\dot{\epsilon}_{II}$  are similarly defined in terms of principal strain rates  $\dot{\epsilon}_1$  and  $\dot{\epsilon}_2$ , the relationship between stress and strain rate described by (2) can be written as

$$\sigma_I = 2\zeta\dot{\epsilon}_I - P/2 \quad \text{and} \quad \sigma_{II} = 2\eta\dot{\epsilon}_{II}. \quad (\text{A3})$$

### A1. Constitutive Law With a Teardrop Yield Curve

[42] Squaring both sides of (A1) with a fatness factor of  $q = 1/2$  and applying the normal flow rule gives

$$\frac{\partial F}{\partial u} = \gamma\dot{\epsilon}_I \quad \text{and} \quad \frac{\partial F}{\partial y} = \gamma\dot{\epsilon}_{II}, \quad (\text{A4})$$

where

$$u = x - a, \quad x = \sigma_I/P, \quad y = \sigma_{II}/P = -(x - a)(1 + x)^{1/2}, \quad (\text{A5})$$

$$F = y^2 - (1 + a)u^2 - u^3 = 0. \quad (\text{A6})$$

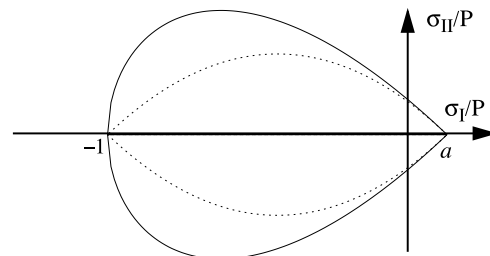


**Figure A1.** Teardrop and lens yield curves in a  $\sigma_I - \sigma_{II}$  coordinate system, with the maximum compressive stress independent of the maximum tensile stress (for teardrop and lens rheologies).

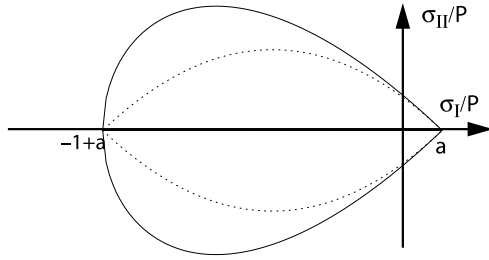


**Figure A2.** Teardrop and lens yield curves in a  $\sigma_I - \sigma_{II}$  coordinate system, with the maximum compressive stress depending on the maximum tensile stress (for teardrop 2 and lens 2 rheologies).

From (A4) and (A6) we get, after some algebra, the following equation

$$9u^2 + [12(1+a) - 4k^2]u + [4(1+a)^2 - 4k^2(1+a)] = 0, \quad (\text{A7})$$

where  $k = \dot{\epsilon}_I/\dot{\epsilon}_{II}$ . For  $k \leq 1$  the solution for (A7) is

$$u = \frac{-[6(1+a) - 2k^2] + 2k\sqrt{k^2 + 3(1+a)}}{9}. \quad (\text{A8})$$

Once  $u$  is determined,  $x$  and  $y$  are determined by (A5). For  $k > 1$ , we set  $x = a$  and  $y = 0$ . The viscosities can be derived from (A3) and (A5) such that

$$\zeta = \frac{\sigma_I + P/2}{2\dot{\epsilon}_I} = \frac{x + 1/2}{2\dot{\epsilon}_I} P, \quad (\text{A9})$$

$$\eta = \frac{\sigma_{II}}{2\dot{\epsilon}_{II}} = \frac{y}{2\dot{\epsilon}_{II}} P = \frac{-(x-a)(1+x)^{1/2}}{2\dot{\epsilon}_{II}} P. \quad (\text{A10})$$

## A2. Constitutive Law With a Parabolic Lens Yield Curve

[43] We similarly apply the normal flow rule on (A2) with a fatness factor of  $q = 1$  and with

$$F = y + u(1+a+u) = 0. \quad (\text{A11})$$

For  $|k| \leq 1$  the solution for (A4) and (A11) is

$$u = (k-1-a)/2. \quad (\text{A12})$$

Once  $u$  is determined we have

$$x = \sigma_I/P = u + a \quad \text{and} \quad y = \sigma_{II}/P = -(x-a)(1+x). \quad (\text{A13})$$

Also, we set  $x = a$ ,  $y = 0$  for  $k > 1$ , and  $x = -1$ ,  $y = 0$  for  $k < -1$ . The viscosities are

$$\zeta = \frac{\sigma_I + P/2}{2\dot{\epsilon}_I} = \frac{x + 1/2}{2\dot{\epsilon}_I} P, \quad (\text{A14})$$

$$\eta = \frac{\sigma_{II}}{2\dot{\epsilon}_{II}} = \frac{y}{2\dot{\epsilon}_{II}} P = \frac{-(x-a)(1+x)}{2\dot{\epsilon}_{II}} P. \quad (\text{A15})$$

What is the best choice for the biaxial tensile stress parameter  $a$  is not clear. In this study, however, the biaxial tensile stress parameter  $a$  is set to 0.05 for either teardrop or lens rheology, which allows biaxial tensile stress comparable to that allowed by the MCE rheology (Figure 1). Setting  $a = 0$ , we obtain the teardrop 1 or lens 1 rheology that does not allow any tensile stress.

[44] Note that, in addition to allowing biaxial tensile stress, teardrop and lens yield curves are also fatter than teardrop 1 and lens 1. In order to single out the effect of incorporating biaxial tensile stress, teardrop 2 and lens 2 (section 3) have been used also for model integrations. Teardrop 2 and lens 2 have the same fatness as teardrop 1 and lens 1, while allowing biaxial tensile stress. A common equation parallel to (A1) for describing teardrop 2 and lens 2 plastic yield curves (Figure A2) can be written as

$$\sigma_{II}/P = -(\sigma_I/P - a)[1 + (\sigma_I/P - a)]^q.$$

The solutions can be similarly derived to be

$$u = \frac{-(6 - 2k^2) + 2k\sqrt{k^2 + 3}}{9}$$

for teardrop 2, and

$$u = (k-1)/2$$

for lens 2.

## Appendix B: Derivation of the Normalized Mechanical Energy Dissipation Rate

[45] The normalized mechanical energy dissipation rate  $M$  described in (9) is determined once the  $\bar{\Delta}$  function is determined. From (A2) and with a  $45^\circ$  rotation of the principal stresses, the total normalized energy dissipation rate can be written as

$$P^{-1}\sigma_{ij}\dot{\epsilon}_{ij} = P^{-1}\sigma_i\dot{\epsilon}_i = 2P^{-1}(\sigma_I\dot{\epsilon}_I + \sigma_{II}\dot{\epsilon}_{II}). \quad (\text{B1})$$

Applying (10) and (A3) leads to

$$P^{-1}\sigma_{ij}\dot{\epsilon}_{ij} = 4(\zeta\dot{\epsilon}_I^2 + \eta\dot{\epsilon}_{II}^2)/P - \dot{\epsilon}_I = \frac{1}{2}(\bar{\Delta} - \dot{\epsilon}_{kk}), \quad (\text{B2})$$

where  $\bar{\Delta} = 8(\zeta\dot{\epsilon}_I^2 + \eta\dot{\epsilon}_{II}^2)/P$ . From (A9), (A10), (A14), (A15), and (B2) we obtain

$$\bar{\Delta} = 4\left[(x+1/2)\dot{\epsilon}_I - (x-a)(1+x)^{1/2}\dot{\epsilon}_{II}\right] \quad (\text{B3})$$

for the teardrop rheologies (teardrop and teardrop 1) and

$$\bar{\Delta} = 4[(x+1/2)\dot{\epsilon}_I - (x-a)(1+x)\dot{\epsilon}_{II}] \quad (\text{B4})$$

for the lens rheologies (lens and lens 1). Similar procedures can be applied for teardrop 2 and lens 2. The corresponding equation for the Mohr-Coulomb part

of the MCE yield curve can be derived from (4) and (B2) such that

$$\bar{\Delta} = 8 \left[ \frac{\dot{\epsilon}_I^2}{2\Delta} + \frac{2\Delta - 1.8\dot{\epsilon}_{kk}}{1.4 \cdot 1.8 \cdot \dot{s} \cdot 2\Delta} \dot{\epsilon}_{II}^2 \right]. \quad (\text{B5})$$

Along the ellipse part of the MCE yield curve,  $\bar{\Delta} = \Delta$ .

[46] **Acknowledgments.** We thank I. Rigor for providing buoy motion, sea level pressure, and surface air temperature data, A. Schweiger and M. Ortmeyer for computer assistance, and B. Tremblay, R. Kwok, and an anonymous reviewer for constructive comments. Submarine ice draft data are provided by the National Snow and Ice Data Center. We gratefully acknowledge the support of NASA (grants NNG04GB03G and NAG5-9334), NSF (grant OPP-0240916), and ONR (grant N00014-99-1-0742).

## References

- Bourke, R. H., and A. S. McLaren (1992), Contour mapping of Arctic Basin ice draft and roughness parameters, *J. Geophys. Res.*, *97*, 17,715–17,728.
- Bryan, K. (1969), A numerical method for the study of the circulation of the world oceans, *J. Comput. Phys.*, *4*, 347–376.
- Colony, R. L., and I. G. Rigor (1993), International Arctic Ocean Buoy Program data report for 1 January 1992–31 December 1992, *Tech. Rep. APL-UW TM 2-93*, 215 pp., Appl. Phys. Lab., Univ. of Wash., Seattle.
- Coon, M. D. (1974), Mechanical behavior of compacted Arctic ice floes, *J. Pet. Technol.*, *26*, 466–470.
- Cox, M. D. (1984), A primitive equation, three-dimensional model of the oceans, *GFDL Ocean Group Tech. Rep. 1*, Geophys. Fluid Dyn. Lab., Princeton, N. J.
- Flato, G. M., and W. D. Hibler III (1995), Ridging and strength in modeling the thickness distribution of Arctic sea ice, *J. Geophys. Res.*, *100*, 18,611–18,626.
- Hibler, W. D., III (1979), A dynamic thermodynamic sea ice model, *J. Phys. Oceanogr.*, *9*, 815–846.
- Hibler, W. D., III (1980), Modeling a variable thickness sea ice cover, *Mon. Weather Rev.*, *1*, 1943–1973.
- Hibler, W. D., III, and K. Bryan (1987), A diagnostic ice-ocean model, *J. Phys. Oceanogr.*, *7*, 987–1015.
- Hibler, W. D., III, and E. Schulson (1997), On modeling sea-ice fracture and flow in numerical investigations of climate, *Ann. Glaciol.*, *25*, 26–32.
- Hibler, W. D., III, and E. Schulson (2000), On modeling anisotropic failure and flow of flawed sea ice, *J. Geophys. Res.*, *105*, 17,105–17,120.
- Hunke, E. C., and J. K. Dukowicz (1997), An elastic-viscous-plastic model for sea ice dynamics, *J. Phys. Oceanogr.*, *27*, 1849–1867.
- Hunke, E. C., and Y. Zhang (1999), A comparison of sea ice dynamics models at high resolution, *Mon. Weather Rev.*, *127*, 396–408.
- Ip, C. F. (1993), Numerical investigation of different rheologies on sea-ice dynamics, Ph.D. thesis, 242 pp., Dartmouth Coll., Hanover, N. H.
- Ip, C. F., W. D. Hibler III, and G. M. Flato (1991), On the effect of rheology on seasonal sea-ice simulations, *Ann. Glaciol.*, *15*, 17–25.
- Menemenis, D., et al. (2005), NASA supercomputer improves prospects for ocean climate research, *Eos Trans. AGU*, *86*(9), 89, 96.
- Overland, J. E., and R. L. Colony (1994), Geostrophic drag coefficients for the central Arctic derived from Soviet drifting station data, *Tellus, Ser. A*, *46*, 75–85.
- Overland, J. E., and C. H. Pease (1988), Modeling ice dynamics of coastal seas, *J. Geophys. Res.*, *93*, 15,619–15,637.
- Parkinson, C. L., and W. M. Washington (1979), A large-scale numerical model of sea ice, *J. Geophys. Res.*, *84*, 311–337.
- Pritchard, R. S. (1975), An elastic-plastic constitutive law for sea ice, *J. Appl. Mech.*, *42*, 379–384.
- Rigor, I. G., R. L. Colony, and S. Martin (2000), Variations in surface air temperature observations in the Arctic, 1979–97, *J. Clim.*, *13*, 896–914.
- Rigor, I. G., J. M. Wallace, and R. L. Colony (2002), On the response of sea ice to the Arctic Oscillation, *J. Clim.*, *15*, 2648–2662.
- Rothrock, D. A. (1975), The mechanical behavior of pack ice, *Annu. Rev. Earth Planet. Sci.*, *3*, 317–342.
- Schulson, E. M. (2001), Brittle failure of ice, *Eng. Fract. Mech.*, *68*, 1839–1887.
- Smith, R. B. (1983), A note on the constitutive law for sea ice, *J. Glaciol.*, *29*, 191–195.
- Stern, H. L., D. A. Rothrock, and R. Kwok (1995), Open water production in Arctic sea ice: Satellite measurements and model parameterizations, *J. Geophys. Res.*, *100*, 20,601–20,612.
- Thorndike, A. S., D. A. Rothrock, G. A. Maykut, and R. Colony (1975), The thickness distribution of sea ice, *J. Geophys. Res.*, *80*, 4501–4513.
- Tremblay, L. B., and L. A. Mysak (1997), Modeling sea ice as a granular material, including the dilatancy effect, *J. Phys. Oceanogr.*, *27*, 2342–2360.
- Zhang, J., and W. D. Hibler III (1997), On an efficient numerical method for modeling sea ice dynamics, *J. Geophys. Res.*, *102*, 8691–8702.
- Zhang, J., and D. A. Rothrock (2000), Modeling Arctic sea ice with an efficient plastic solution, *J. Geophys. Res.*, *105*, 3325–3338.
- Zhang, J., and D. A. Rothrock (2001), A thickness and enthalpy distribution sea-ice model, *J. Phys. Oceanogr.*, *31*, 2986–3001.
- Zhang, J., and D. A. Rothrock (2003), Modeling global sea ice with a thickness and enthalpy distribution model in generalized curvilinear coordinates, *Mon. Weather Rev.*, *131*, 681–697.
- Zhang, J., W. D. Hibler III, M. Steele, and D. A. Rothrock (1998), Arctic ice-ocean modeling with and without climate restoring, *J. Phys. Oceanogr.*, *28*, 191–217.
- Zhang, J., D. A. Rothrock, and M. Steele (2000), Recent changes in Arctic sea ice: The interplay between ice dynamics and thermodynamics, *J. Clim.*, *13*, 3099–3114.

D. A. Rothrock and J. Zhang, Polar Science Center, Applied Physics Laboratory, College of Ocean and Fishery Sciences, University of Washington, Seattle, WA 98105, USA. (zhang@snark.apl.washington.edu)